


Trap-state suppression and band-like transport in bilayer-type organic semiconductor ultrathin single crystals

Takamasa Hamai¹,* Satoru Inoue¹, Shunto Arai¹, and Tatsuo Hasegawa¹
Department of Applied Physics, The University of Tokyo, Tokyo 113-8656, Japan

 (Received 26 March 2020; accepted 22 May 2020; published 2 July 2020)

Fundamental study of the carrier transport in both the channel layer and the electrode-channel contact of organic semiconductor crystals is indispensable for achieving high-performance organic field-effect transistors. In this paper, we report the temperature-dependent carrier transport of high-mobility organic semiconductors called 2-decyl-7-phenyl-[1]benzothieno[3,2-*b*][1]benzothiophene (Ph-BTBT-C10) and 3-decyl-9-phenyl-[1]benzothieno[3,2-*b*]naphtho[2,3-*b*]thiophene (Ph-BTNT-C10). The use of single-crystal films with controlled bilayer-number thickness enabled the simultaneous study of intralayer and interlayer transport at cryogenic temperatures. Four-probe measurement of two-bilayer- and three-bilayer-thick films of Ph-BTBT-C10 suggests that the access resistance is dominated by tunneling transport across the insulating alkyl-chain layers. Single-crystal thin-film transistors of these materials showed band-like carrier transport down to 80 K and the carrier mobility of Ph-BTBT-C10 reached $34 \text{ cm}^2/\text{V s}$. Detailed analysis of the low-temperature characteristics revealed small activation energy of approximately 5 meV and a sharp distribution of band tail states. These findings suggest that high crystallinity owing to the bilayer-type crystal structure effectively suppresses the localization of gate-induced carriers.

DOI: [10.1103/PhysRevMaterials.4.074601](https://doi.org/10.1103/PhysRevMaterials.4.074601)

I. INTRODUCTION

Organic semiconductors (OSCs) are the most promising materials for the active layer of high-performance field-effect transistors (FETs) in printed and flexible electronics applications. The conducting carriers in the FETs are driven at the semiconductor/gate-dielectric interface, so that the two-dimensional (2D) crystal growth of OSC is indispensable for fabricating high-performance organic FETs. In particular, it has recently been shown that alkyl-substituted OSC molecules are the most promising material class, as they spontaneously form thin-flake-like single crystals from OSC solution [1–3]. Using appropriate solution processes, these materials can afford high-performance organic FETs with mobilities of up to $10 \text{ cm}^2/\text{V s}$ [4–8] and open up possibilities for high-speed-operated devices [9–11].

To achieve higher device performance, it is necessary to precisely model how carriers are transported inside OSC layers. Several groups have reported a correlation between high mobility and band-like carrier transport in alkyl-substituted OSC materials [12–15]. The band-like transport can be easily characterized by the negative temperature dependence of carrier mobility caused by the suppression of electron-phonon scattering at low temperatures. However, the band-like region ($\partial\mu/\partial T < 0$) is restricted to a high temperature range, even in high-mobility OSC materials. The characteristic temperature T^* is defined to separate the band-like and activated regions ($\partial\mu/\partial T > 0$): Typical T^* values are 220 K for C10-DNBDT-NW ($\sim 16 \text{ cm}^2/\text{V s}$ at 300 K) [13], 190 K for F4-TCNQ ($\sim 3 \text{ cm}^2/\text{V s}$ at 300 K) [12], 180 K for C10-DNTT ($\sim 10 \text{ cm}^2/\text{V s}$ at 300 K) [14], and 90 K for rubrene

($\sim 15 \text{ cm}^2/\text{V s}$ at 300 K) [15]. T^* represents the temperature at which the gate-induced carriers begin to be localized by extrinsic disorder [12,16]. Carrier transport should be disturbed by extrinsic disorder that works as shallow trap states even at room temperature [12,17–19]. Hence, a small T^* should correspond to an indicator for obtaining high-mobility organic FETs.

Another crucial issue for improving FET characteristics is large parasitic resistance (R_p). For example, Klauk discussed that the R_p should be lower than $10 \Omega \text{ cm}$ to realize 1-GHz operation as the R_p critically affects high-speed device performance [20]. However, no organic FETs have met this criteria so far; the smallest R_p value is reported as several tens of $\Omega \text{ cm}$ [9,10]. To achieve the smaller R_p , it is necessary to understand the origin of relatively large R_p in organic FETs.

Previously we reported high carrier mobility ($\sim 10 \text{ cm}^2/\text{V s}$) and layer-number-dependent nonlinear R_p in single-crystal organic FETs based on an alkyl-substituted OSC called 2-decyl-7-phenyl-[1]benzothieno[3,2-*b*][1]benzothiophene [Ph-BTBT-C10, Fig. 1(a)] [6]. The material exhibits fairly high layered crystallinity owing to the formation of molecular-bilayer structure where the unsymmetrical molecule forms a head-to-head alignment. It was shown that high mobility is obtained by high layered crystallinity, although it is accompanied by a large access resistance originating from the insulating alkyl-chain layers. It was discussed that the access resistance across the insulating alkyl-chain layer should dominate the R_p in the single-crystal FET. However, intrinsic carrier transport in both intralayer and interlayer directions has not yet been revealed.

Here we investigated temperature-dependent transistor characteristics of single-crystal organic FETs composed

*hamai@hsgw.t.u-tokyo.ac.jp

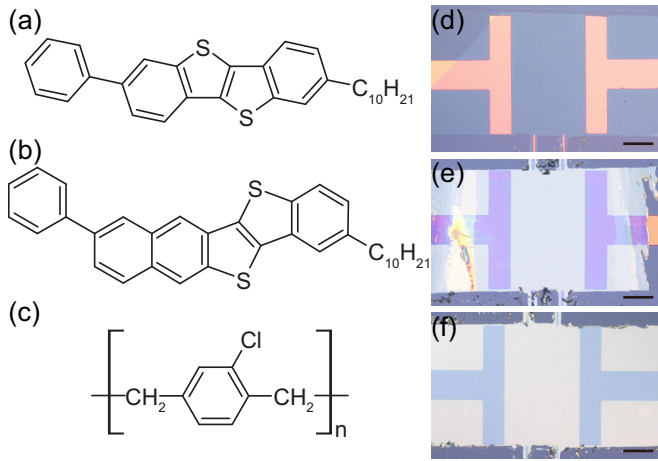


FIG. 1. (a)–(c) Molecular structures of (a) Ph-BTBT-C10, (b) Ph-BTNT-C10, and (c) parylene C. (d)–(f) Optical micrographs of (d) device A, (e) device B, and (f) device C. Scale bars show 100 μm . The thickness of parylene layers are measured to be 26 and 40 nm for (e) and (f), respectively.

of Ph-BTBT-C10 and 3-decyl-9-phenyl-[1]benzothieno[3,2-*b*]naphtho[2,3-*b*]thiophene [Ph-BTNT-C10, Fig. 1(b)], a high-

performance OSC material with the same crystal structure as Ph-BTBT-C10 [21]. We first revealed by four-probe measurements that the access resistance is nearly temperature independent, as it originates from the tunneling effect across the insulating alkyl-chain layers in single-crystal organic FETs. We found that the carrier mobilities in all the measured devices of both Ph-BTBT-C10 and Ph-BTNT-C10 increased with decreasing temperature down to 80 K, and reached a maximum value at 34 $\text{cm}^2/\text{V s}$ at 80 K in Ph-BTBT-C10. The temperature dependence of mobility obeys the power law in high-temperature ranges, while it shows thermal-activation-type behavior in low-temperature ranges. Analyses of the low-temperature characteristics revealed a shallow trap density of states. We discuss the band-like behaviors and the distribution of low-energy trap states in terms of both the highly layered-crystalline OSC and the semiconductor/gate-dielectric interfaces.

II. FABRICATION OF ORGANIC FETs AND ROOM-TEMPERATURE CHARACTERISTICS

We fabricated and used three types of devices composed of different OSC, layer number, or gate-dielectric surfaces: (A) single-crystal organic FETs with two-bilayer-thick [device A, Fig. 1(d)] and three-bilayer-thick Ph-BTBT-C10 on a SiO_2

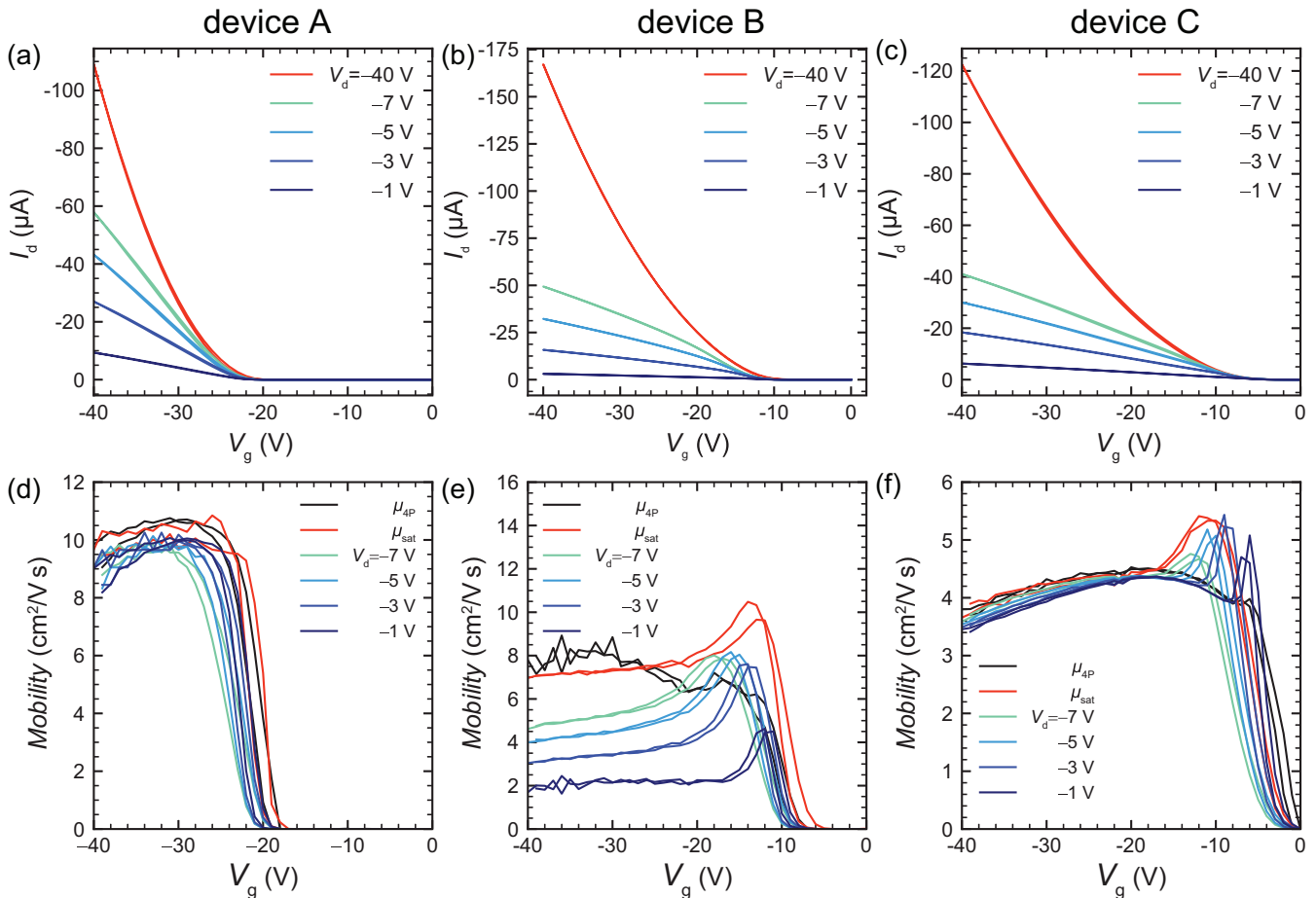


FIG. 2. Transfer characteristics of single-crystal transistors at 300 K. (a)–(c) I_d - V_g characteristics of (a) device A, (b) device B, and (c) device C. (d)–(f) V_g dependence of device mobility of (d) device A, (e) device B, and (f) device C.

gate dielectric surface (device A'); (B) three-bilayer-thick Ph-BTBT-C10 on a parylene C gate-dielectric surface [device B, Fig. 1(e)], and (C) two-bilayer-thick Ph-BTNT-C10 on a parylene C gate-dielectric surface [device C, Fig. 1(f)]. We used highly doped silicon wafers with 100-nm-thick thermal oxide layers as base substrate. The gate-dielectric surfaces of devices B and C were passivated with chemical vapor deposited parylene C [Fig. 1(c)] to reduce interface states [22]. The thickness of parylene layers was measured by atomic force microscopy to be 24 and 40 nm for devices B and C, respectively.

The OSC single-crystal films were fabricated by the blade coating technique at room temperature [6]. We obtained layer-number-controlled and relatively large single-crystal domains with an area more than mm^2 order. Single crystallinity was confirmed by crossed-Nicols polarized optical microscopy observation. Chlorobenzene solutions of Ph-BTBT-C10 or Ph-BTNT-C10 at concentrations of 0.1 wt% were used for the fabrication of all the devices. The sweep rate of the blade was set at $3.5 \mu\text{m}/\text{sec}$. $F_4\text{-TCNQ}$ (5 nm)/Au (30 nm) electrodes were vacuum deposited onto the OSC films through a shadow mask as source and drain electrodes with top contact geometry. Each channel was formed to be aligned with an optical principal axis (i.e., crystallographic a or b axis) under the polarized optical microscope. Channel geometry ($250 \mu\text{m}$ in length and $400 \mu\text{m}$ in width) was defined by subsequent trimming of the semiconductor layer with a micromanipulator.

Figure 2 shows the I_d - V_g characteristics of fabricated organic FETs at 300 K. We obtained hysteresis-free characteristics and high mobility as $10 \text{ cm}^2/\text{Vs}$ in device A, $7 \text{ cm}^2/\text{Vs}$ in device B, and $4 \text{ cm}^2/\text{Vs}$ in device C. The V_g independence of field-effect mobility in wide V_g range [Figs. 2(d)–2(f)] is indicative of the high quality of semiconductor layer and source/drain contact [23–25]. This result excludes the possibility of mobility overestimation due to nonideal transistor characteristics in spite of the large threshold voltages [23]. Threshold voltage was as high as -20 V in device A [Fig. 2(a)] but decreased by passivating interface states with parylene C [Fig. 2(b)] and replacing Ph-BTBT-C10 with Ph-BTNT-C10 [Fig. 2(c)], which has shallower highest occupied molecular orbital [21]. We consider that the distribution of device mobility between each device should be caused by the anisotropy of the channel single-crystal layer between along a and b axes. Actually, it was reported that in-plane anisotropy of mobility in single-crystal thin films of Ph-BTBT-C6 was estimated at approximately 1.5 times [26]. Nonetheless, it is expected that such an anisotropy or the absolute value of mobility should not affect the temperature dependence of mobility that will be discussed later.

III. ACCESS RESISTANCE DUE TO ALKYL CHAIN LAYER

The device mobility of device B showed large V_d dependence, although those of device A and C were independent of V_d . The device mobility of device B at $V_d = -1 \text{ V}$ was as small as $2 \text{ cm}^2/\text{Vs}$ [Fig. 2(e)]. The difference between devices A and C, and device B was the layer-number thickness. The notable V_d dependence of mobility in device B was owing to nonlinear access resistance in the thicker (three-bilayer-thick) film [6]. This result is consistent with the previous work,

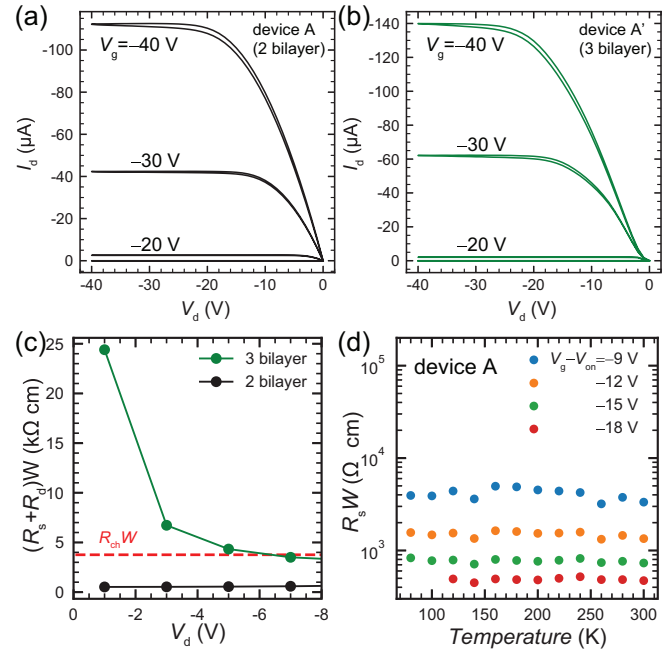


FIG. 3. (a), (b) Output characteristics of (a) device A and (b) device A'. (c) Width-normalized access resistance of device A (black) and device A' (green) as a function of V_d at $V_g = -40 \text{ V}$. Width-normalized channel resistance of device A at $V_g = -40 \text{ V}$ is shown by red broken line. (d) Temperature dependence of $R_s W$ of device A measured at $V_d = -1 \text{ V}$.

where carrier transport was dominated by nonlinear direct tunneling transport across the insulating alkyl-chain layer [27,28]. The three-bilayer-thick FET exhibited higher access resistance than the two-bilayer-thick FET.

To elucidate how the excessive layer affects the FET characteristics, we compared the access resistance of devices A and A'. Figures 3(a) and 3(b) show the I_d - V_d characteristics of devices A and A', respectively. We successfully demonstrated that only one additional bilayer causes considerable nonlinear behavior in the small V_d region (see Fig. S1 of the Supplemental Material) [29], although they showed almost the same I_d in the saturation region ($\sim \mu_{\text{sat}}$). We employed a four-probe technique to obtain the potential drop at the source and drain electrode to estimate the access resistance. Figure 3(c) shows the V_d dependence of the width-normalized parasitic resistance ($R_p W$), the sum of the parasitic resistance of the source electrode (R_s), and the drain electrode (R_d), at 300 K. The parasitic resistance of the source and drain electrodes were estimated with the relation $R_{s,d} = \Delta V_{s,d}/I_d$, where $\Delta V_{s,d}$ denotes the potential drop between channel layer and source or drain electrode [6]. The small and nearly V_d -independent R_p ($520 \Omega \text{ cm}$ at $V_d = -1 \text{ V}$) of device A was consistent with the Ohmic-like characteristics of this transistor [Figs. 2(a) and 2(d)], and parasitic resistance due to the OSC/electrode interface such as the Schottky barrier can be ignored. Meanwhile, the R_p of device A' showed negative V_d dependence and reached $24 \text{ k}\Omega \text{ cm}$ at $V_d = -1 \text{ V}$. It is clear that the large and nonlinear access resistance, that only appeared in the thick OSC layer (three bilayer), caused the nonlinear behavior of device A' shown in Figs. 2(b) and 2(e). Note that one-bilayer

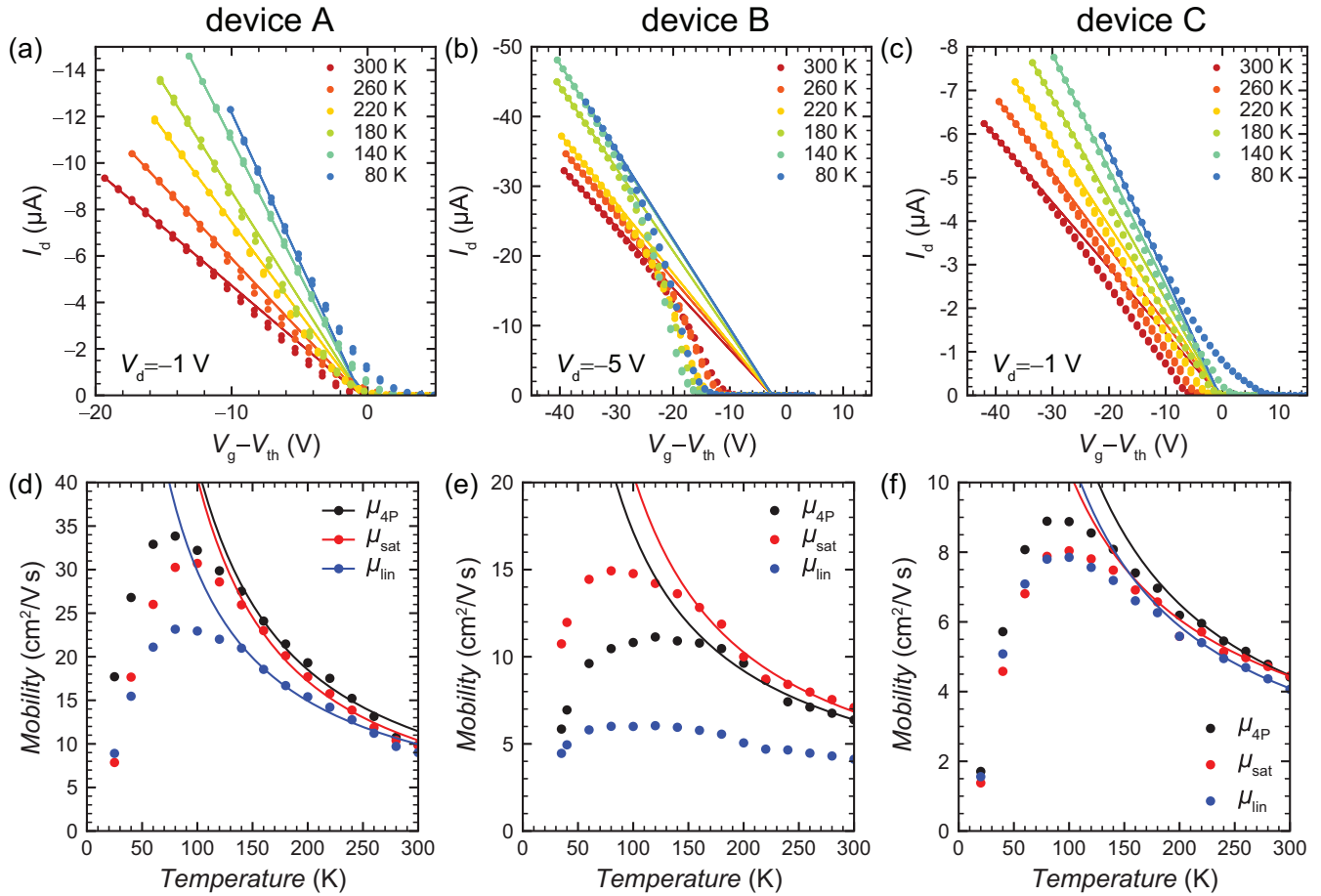


FIG. 4. Band-like carrier transport in bilayer-type OSCs. (a)–(c) Temperature dependence of I_d - V_g characteristics of (a) device A, (b) device B, and (c) device C. (d)–(f) Temperature dependence of device mobility of (d) device A, (e) device B, and (f) device C. All of the solid curves in (d)–(f) show the relationship of $\mu \propto T^{-\alpha}$, where α was distributed within a range of $0.8 < \alpha < 1.4$.

organic FETs are not discussed here because the too thin OSC layer can be easily damaged during the deposition of electrode metal [6,9].

To investigate the mechanism of the nonlinear interlayer transport in Ph-BTBT-C10, we measured the temperature dependence of access resistance. Figure 3(d) shows the temperature dependence of R_s in device A as a function of $V_g - V_{on}$ (onset voltage). We confirmed that R_s has a negligible temperature dependence at least above 80 K. The temperature-independent resistance is the clear evidence that the access resistance in single-crystal film of Ph-BTBT-C10 is dominated by tunneling transport [6,28,30,31]. Note that the nonlinear access resistance does not affect the mobility in saturation region [Fig. 2(e)]. When the applied V_d is sufficient to cause pinch-off, the access resistance becomes small enough compared to the resistance due to the pinch-off point, which is the origin of “saturation” behavior of the drain current. Therefore, the mobility measured in the saturation region was consistent with that measured by the four-probe technique, which should reflect the intrinsic value of the transistor [28].

IV. BAND-LIKE CARRIER TRANSPORT

To investigate the intralayer carrier transport mechanism, we studied the temperature dependence of the transistor

characteristics by cooling the single-crystal organic FETs down to cryogenic temperature ($\sim 20\text{ K}$). Figures 4(a)–4(c) show the temperature dependence of the I_d - V_g characteristics. The mobility evaluated from the slopes increased with decreasing temperature in a very wide temperature range of 80–300 K in all devices we measured (see Fig. S2 of the Supplemental Material for the μ - V_g relation) [29]. This is unambiguous evidence of band-like carrier transport in Ph-BTBT-C10 and Ph-BTNT-C10 single-crystal films. Here we plotted the transfer characteristics against $V_g - V_{th}$ for simplicity as V_{th} increased with decreasing temperature (see Fig. S3) [29]. The increase in V_{th} at lower temperatures should originate from carrier trapping of gate-induced carriers by relatively shallow trap states.

The temperature dependence of carrier mobility is summarized in Figs. 4(d)–4(f). The four-probe mobility of device A reached $34\text{ cm}^2/\text{Vs}$ at 80 K. The increase in mobility can be fitted with the power law ($\mu \propto T^{-\alpha}$) in the band-like regime as shown in the solid curves. The exponent factors α in the power-law fitting in our experiment range between 0.8 and 1.4. These values are in good agreement with previously reported values for other high-mobility OSC crystals (0.9–1.3) [12,13]. The numerical calculation based on the transient localization scenario predicted that α should be approximate unity in two-dimensional transport [32,33].

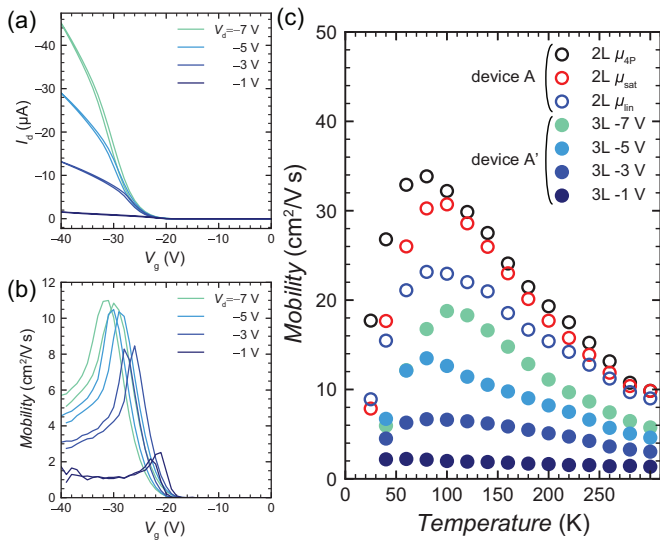


FIG. 5. (a) I_d - V_g characteristics of device A' at 300 K. (b) μ - V_g relationship of device A' at 300 K. (c) Temperature dependence of device mobility. Open and filled circles denote the mobility of device A and device A', respectively.

Based on the observed exponent factors and the transient localization scenario, the high mobility in Ph-BTBT-C10 and Ph-BTNT-C10 can be understood as efficient carrier transport through the delocalized molecular wave functions, which may be the result of the small anisotropy of transfer integral [2] and the suppression of intermolecular vibration by the long-alkyl-chain substitution [12,34].

In device A', device characteristics at room temperature are affected by the tunnel resistance as shown in Fig. 3. Here we show how tunnel resistance hinders the increase in device mobility at low temperatures. Figure 5(a) shows the I_d - V_g characteristics of device A', and Fig. 5(b) shows the corresponding μ - V_g relation. We can clearly see that device mobility is suppressed at low V_d owing to nonlinear access resistance. We measured the mobility of device A' down to cryogenic temperature, which is summarized in Fig. 5(c). In this plot, we show the mobility of device A' at various V_d and that of device A for comparison. For large V_d such as -7 V, the mobility of device A' increased up to $19 \text{ cm}^2/\text{V s}$ with decreasing temperature. This temperature dependence was qualitatively consistent with device A. However, when we decrease V_d , not only the value of the mobility but also the increase of mobility was suppressed. During cooling from 300 to 100 K, the device mobility at $V_d = -7$ V increased three times while that at $V_d = -1$ V increased only 1.5 times. For small V_d such as -1 V, the tunneling-based access resistance in device A' is too large compared to the channel resistance (R_{ch}) for investigating the intrinsic temperature dependence of R_{ch} . When larger V_d was applied, the access resistance decreased and hence the extrinsic temperature dependence approached the intrinsic characteristics of channel layer that were captured with device A.

Here we note that the electrical characteristics of our single-crystal organic FETs do not seem to be affected by the cooling process. We confirmed that all of the devices shown in this paper exhibited negligible degradation in the

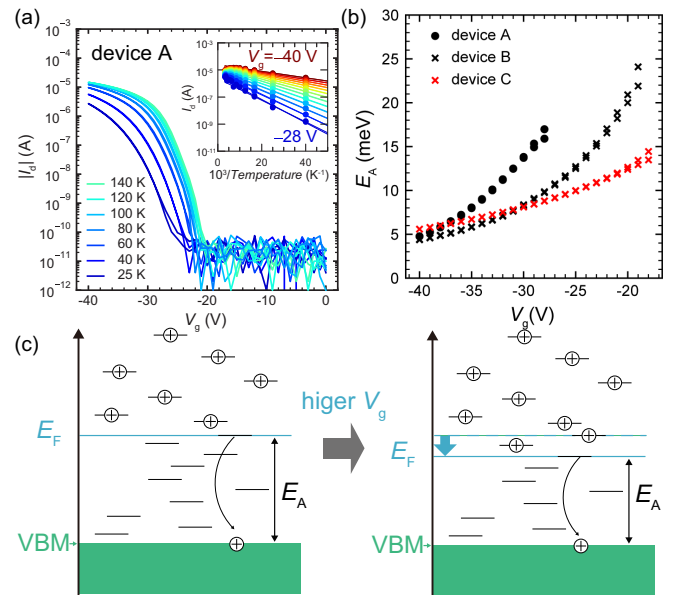


FIG. 6. Activated behavior at low-temperature region. (a) Temperature dependence of I_d - V_g characteristics of device A below 140 K plotted in a semilogarithmic scale. Inset shows an Arrhenius plot of the same data. (b) Activation energies estimated from the Arrhenius plot. (c) Schematic of the relationship between E_A and V_g .

room-temperature characteristics after the low-temperature measurements (e.g., see Fig. S4 [29]).

V. SHALLOW TRAP DENSITY OF STATES

Our organic FETs based on Ph-BTBT-C10 and Ph-BTNT-C10 single crystals showed a high mobility and band-like mobility-temperature relationship over the wide temperature range $80 \text{ K} < T < 300 \text{ K}$. The characteristic temperature T^* was lower than any other organic FETs and even comparable to that of vacuum-gap rubrene transistor [15]. As reported in earlier works based on both organic [12,15,35] and inorganic FETs [19], the lower T^* represents the smaller disorder density. Here we focus on the mobility-temperature relationship of the lower temperature range ($T < 80 \text{ K}$) to evaluate the quality of our single-crystal FETs.

All of our single-crystal organic FETs showed a rapid decrease in mobility below 80 K, which was accompanied by an increase in V_{on} [Fig. 6(a)]. This transition from band-like transport ($\partial\mu/\partial T < 0$) to activated behavior ($\partial\mu/\partial T > 0$) can be explained by shallow trap states [17]. In general, it is considered that the Fermi energy (E_F) of organic FETs are not located inside the valence band even with high V_g because of trap states around valence-band maximum (VBM). That means that the number of trap states is greater than that of gate-induced carriers ($\sim 10^{13}/\text{cm}^2$). A schematic energy diagram for gate-induced carriers in organic FETs can be seen in Fig. 6(c). This indicates that trapped carriers around E_F are mobile only if their thermal energy is sufficient to overcome the trap energy at E_F .

We estimated the trap energy at E_F , or activation energy (E_A) in our transistor in an Arrhenius plot. Figure 6(b) shows the E_A - V_g relationship obtained from the slope of the inset of

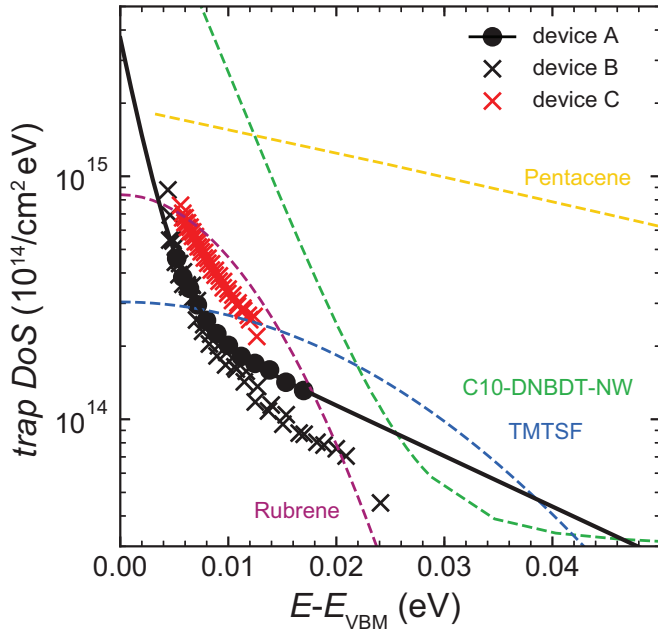


FIG. 7. Distribution of trap DoS extracted from V_g -dependent activation energies. Solid curve shows the fitting curve for the results of device A. Literature data (broken curves) were obtained from pentacene [35], C10-DNBDT-NW [36], TMTSF [37], Rubrene [15].

Fig. 6(a). We found that the very small E_A of approximately 5 meV enabled a band-like mobility-temperature relationship (Fig. 4) down to 80 K (7 meV). The negative $|V_g|$ dependence of E_A is consistent with the schematic [Fig. 6(c)]. The larger the V_g applied, the more carriers are induced to fill the shallower trap states to move the E_F closer to the VBM.

To evaluate the number of trap states in our organic FET, we extracted the trap density of states (DoS) from the V_g dependence of E_A [36,37]. By approximating the Fermi-Dirac distribution as a step function, we defined the trap DoS [$D(E_F)$] by the following relation:

$$D(E_F) = \frac{\Delta N(E_F)}{\Delta E_F} \quad (1)$$

where $N(E_F)$ denote the hole density. Experimentally, the change in hole density is induced by the change in gate voltage ΔV_g as $\Delta N(E_F) = C_i \Delta V_g / e$ (e : the elementary charge). The activation energy can be approximated as the difference between E_F and the energy of VBM E_{VBM} , i.e., $E_A = E_F - E_{VBM}$. By replacing the difference quotients in Eq. (1) with its respective derivative, we obtain

$$D(E_F) = \frac{C_i}{e} \left(\frac{dE_A}{dV_g} \right)^{-1}. \quad (2)$$

Figure 7 shows the trap DoS distribution extracted from the data shown in Fig. 6(b). We also plotted literature values of single-crystal organic FETs for comparison [15,37–39]. The trap DoS of organic FETs composed of Ph-BTBT-10 or Ph-BTNT-C10 was distributed across a narrow energy range (~ 10 meV) and was about ten times smaller than pentacene, and C10-DNBDT-NW in the shallowest region. The obtained values were comparable to those of the air-gap rubrene transistor [15] despite the large V_{th} . We found that the distribution of trap DoS evaluated from activation energy can be fitted with a double-exponential function [Eq. (3)]:

$$\text{trap DoS}(E) = D_1 e^{-(E/E_1)} + D_2 e^{-(E/E_2)}. \quad (3)$$

The fitting parameters are summarized in Table I and the fitting curve of device A is shown by the solid line in Fig. 7 as a representative. The excellent consistency between the experiment and the double-exponential function implies that there are two trap sources with different characteristic energies, which depend on semiconductor material and dielectric surface.

According to Bacalis *et al.* [40], the characteristic energy of the exponentially decaying tail state is connected to the energetic disorder in the semiconductor. The large difference in E_2 between FET with SiO_2 dielectric (21 meV) and that with parylene/ SiO_2 hybrid dielectric (11 meV) implies that the thin parylene layer effectively passivated random potential due to the silanol group on the surface of SiO_2 . It is noteworthy that we obtained very small T^* even with the FET with bare SiO_2 dielectric. According to Janneck *et al.*, the octyl side group of C_8 -BTBT is sufficient to passivate the SiO_2 dielectric surface [41]. We considered that in our Ph-BTBT-C10 organic FETs, the decyl chains also acted as weak passivating layers to decouple the channel layer from the disorders due to dielectric surface to suppress the shallow trap density. Comparison of D_2 between Ph-BTBT-C10 and Ph-BTNT-C10 suggests that the bent molecular structure might make Ph-BTNT-C10 more prone to crystal disorder than Ph-BTBT-C10. The very narrow trap DoS observed in organic FETs with three different combinations of OSC and dielectric layer suggests that the bilayer-type herringbone packing, which is a common feature of Ph-BTBT-C10 and Ph-BTNT-C10, strongly suppresses energetic disorders such as crystal defects and concomitant localization of carriers.

VI. CONCLUSION

We measured the temperature-dependent transistor characteristics of single-crystal films composed of high-performance bilayer-type OSC materials Ph-BTBT-C10 and Ph-BTNT-C10. We observed a band-like mobility-temperature relationship in the widest temperature range among organic FETs, and the mobility of Ph-BTBT-C10 FET with a SiO_2 gate dielectric reached $34 \text{ cm}^2/\text{Vs}$ at 80 K. We also found that

TABLE I. Parameters of trap DoS distribution.

	$D_1(10^{14}/\text{cm}^2 \text{ eV})$	$E_1(\text{meV})$	$D_2(10^{14}/\text{cm}^2 \text{ eV})$	$E_2(\text{meV})$	Total ($10^{12}/\text{cm}^2$)
Device A	34	1.9	3.0	21	13
Device B	72	1.5	4.0	11	15
Device C	87	1.4	12	7.6	21

the wide band-like region is the result of the small activation energy of 5 meV. four-probe measurements of two-bilayer FET and three-bilayer FET revealed that alkyl chain layers cause temperature-independent tunnel resistance. Although two-bilayer organic FET showed small parasitic resistance of 520 Ω cm, three-bilayer organic FET showed a 50 times larger parasitic resistance at small V_d owing to the nonlinear tunnel resistance. The V_g -independent high mobility and small trap DoS were indicative of a clean active layer even with a nontreated SiO₂ interface. Bilayer-type OSCs would be a promising platform for both low-voltage and high-frequency organic FETs and further study of intrinsic carrier transport mechanisms in organic semiconductors is warranted.

ACKNOWLEDGMENTS

We thank K. Miyagawa and Y. Okamoto for their technical assistance. We also thank K. Kanoda for valuable discussion. We are grateful to Nippon Kayaku Co., Ltd., for providing BTBT. A part of this work was supported by “Nanotechnology Platform Japan” of the Ministry of Education, Culture, Sports, Science and Technology (MEXT) in Takeda Cleanroom with help of Nanofabrication Platform Center of the VLSI Design and Education Center (VDEC), the University of Tokyo, Japan. This work was partially supported by JST CREST Grant No. JPMJCR18J2 and JSPS KAKENHI Grant No. JP18H03875, Japan.

-
- [1] H. Minemawari, J. Tsutsumi, S. Inoue, T. Yamada, R. Kumai, and T. Hasegawa, *Appl. Phys. Express* **7**, 091601 (2014).
- [2] S. Inoue, H. Minemawari, J. Tsutsumi, M. Chikamatsu, T. Yamada, S. Horiuchi, M. Tanaka, R. Kumai, M. Yoneya, and T. Hasegawa, *Chem. Mater.* **27**, 3809 (2015).
- [3] H. Minemawari, M. Tanaka, S. Tsuzuki, S. Inoue, T. Yamada, R. Kumai, Y. Shimoi, and T. Hasegawa, *Chem. Mater.* **29**, 1245 (2017).
- [4] H. Minemawari, T. Yamada, H. Matsui, J. Tsutsumi, S. Haas, R. Chiba, R. Kumai, and T. Hasegawa, *Nature (London)* **475**, 364 (2011).
- [5] C. Mitsui, T. Okamoto, M. Yamagishi, J. Tsurumi, K. Yoshimoto, K. Nakahara, J. Soeda, Y. Hirose, H. Sato, A. Yamano, T. Uemura, and J. Takeya, *Adv. Mater.* **26**, 4546 (2014).
- [6] T. Hamai, S. Arai, H. Minemawari, S. Inoue, R. Kumai, and T. Hasegawa, *Phys. Rev. Appl.* **8**, 054011 (2017).
- [7] Z. Zhang, B. Peng, X. Ji, K. Pei, and P. K. L. Chan, *Adv. Funct. Mater.* **27**, 1703443 (2017).
- [8] R. Janneck, N. Pilet, S. P. Bommanaboyena, B. Watts, P. Heremans, J. Genoe, and C. Rolin, *Adv. Mater.* **29**, 1703864 (2017).
- [9] A. Yamamura, S. Watanabe, M. Uno, M. Mitani, C. Mitsui, J. Tsurumi, N. Isahaya, Y. Kanaoka, T. Okamoto, and J. Takeya, *Sci. Adv.* **4**, eaao5758 (2018).
- [10] J. W. Borchert, B. Peng, F. Letzkus, J. N. Burghartz, P. K. L. Chan, K. Zojer, S. Ludwigs, and H. Klauk, *Nat. Commun.* **10**, 1119 (2019).
- [11] A. Yamamura, T. Sakon, K. Takahira, T. Wakimoto, M. Sasaki, T. Okamoto, S. Watanabe, and J. Takeya, *Adv. Funct. Mater.* **30**, 1909501 (2020).
- [12] N. A. Minder, S. Lu, S. Fratini, S. Ciuchi, A. Facchetti, and A. F. Morpurgo, *Adv. Mater.* **26**, 1254 (2014).
- [13] J. Tsurumi, H. Matsui, T. Kubo, R. Häusermann, C. Mitsui, T. Okamoto, S. Watanabe, and J. Takeya, *Nat. Phys.* **13**, 994 (2017).
- [14] B. Peng, S. Huang, Z. Zhou, and P. K. L. Chan, *Adv. Funct. Mater.* **27**, 1700999 (2017).
- [15] W. Xie, K. A. McGarry, F. Liu, Y. Wu, P. P. Ruden, C. J. Douglas, and C. D. Frisbie, *J. Phys. Chem. C* **117**, 11522 (2013).
- [16] Y. Mei, P. J. Diemer, M. R. Niazi, R. K. Hallani, K. Jarolimek, C. S. Day, C. Risko, J. E. Anthony, A. Amassian, and O. D. Jurchescu, *Proc. Natl. Acad. Sci. USA* **114**, E6739 (2017).
- [17] V. Podzorov, E. Menard, J. A. Rogers, and M. E. Gershenson, *Phys. Rev. Lett.* **95**, 226601 (2005).
- [18] S. S. Li, *Solid State Electron.* **20**, 609 (1978).
- [19] D. Long and J. Myers, *Phys. Rev.* **115**, 1107 (1959).
- [20] H. Klauk, *Adv. Electron. Mater.* **4**, 1700474 (2018).
- [21] S. Inoue, S. Shinamura, Y. Sadamitsu, S. Arai, S. Horiuchi, M. Yoneya, K. Takimiya, and T. Hasegawa, *Chem. Mater.* **30**, 5050 (2018).
- [22] S. Kumagai, A. Yamamura, T. Makita, J. Tsurumi, Y. Y. Lim, T. Wakimoto, N. Isahaya, H. Nozawa, K. Sato, M. Mitani, T. Okamoto, S. Watanabe, and J. Takeya, *Sci. Rep.* **9**, 15897 (2019).
- [23] H. H. Choi, K. Cho, C. D. Frisbie, H. Sirringhaus, and V. Podzorov, *Nat. Mater.* **17**, 2 (2018).
- [24] E. G. Bittle, J. I. Basham, T. N. Jackson, and O. D. Jurchescu, *Nat. Commun.* **7**, 10908 (2016).
- [25] T. Uemura, C. Rolin, T.-H. Ke, P. Fesenko, J. Genoe, P. Heremans, and J. Takeya, *Adv. Mater.* **28**, 151 (2016).
- [26] S. Arai, S. Inoue, T. Hamai, R. Kumai, and T. Hasegawa, *Adv. Mater.* **30**, 1707256 (2018).
- [27] J. G. Simmons, *J. Appl. Phys.* **34**, 1793 (1963).
- [28] T. Hamai, S. Arai, and T. Hasegawa, *J. Mater. Res.* **33**, 2350 (2018).
- [29] See Supplemental Material at <http://link.aps.org/supplemental/10.1103/PhysRevMaterials.4.074601> for supplemental figures.
- [30] W. Wang, T. Lee, and M. A. Reed, *Phys. Rev. B* **68**, 035416 (2003).
- [31] A. Salomon, T. Boecking, C. K. Chan, F. Amy, O. Girshevitz, D. Cahen, and A. Kahn, *Phys. Rev. Lett.* **95**, 266807 (2005).
- [32] S. Fratini, D. Mayou, and S. Ciuchi, *Adv. Funct. Mater.* **26**, 2292 (2016).
- [33] S. Fratini, S. Ciuchi, D. Mayou, G. T. De Laissardière, and A. Troisi, *Nat. Mater.* **16**, 998 (2017).
- [34] S. Tanaka, K. Miyata, T. Sugimoto, K. Watanabe, T. Uemura, J. Takeya, and Y. Matsumoto, *J. Phys. Chem. C* **120**, 7941 (2016).
- [35] N. A. Minder, S. Ono, Z. Chen, A. Facchetti, and A. F. Morpurgo, *Adv. Mater.* **24**, 503 (2012).

- [36] D. V. Lang, X. Chi, T. Siegrist, A. M. Sergent, and A. P. Ramirez, *Phys. Rev. Lett.* **93**, 086802 (2004).
- [37] W. L. Kalb and B. Batlogg, *Phys. Rev. B* **81**, 035327 (2010).
- [38] S. Watanabe, H. Sugawara, R. Häusermann, B. Blütle, A. Yamamura, T. Okamoto, and J. Takeya, *Commun. Phys.* **1**, 37 (2018).
- [39] H. Xie, H. Alves, and A. F. Morpurgo, *Phys. Rev. B* **80**, 245305 (2009).
- [40] N. Bacalis, E. N. Economou, and M. H. Cohen, *Phys. Rev. B* **37**, 2714 (1988).
- [41] R. Janneck, P. Heremans, J. Genoe, and C. Rolin, *Adv. Mater. Interfaces* **5**, 201800147 (2018).